Design and measurements of an electrically small, broad bandwidth, non-Foster circuit-augmented protractor antenna

Ning Zhu and , and Richard W. Ziolkowski

Citation: Appl. Phys. Lett. **101**, 024107 (2012); doi: 10.1063/1.4736996
View online: http://dx.doi.org/10.1063/1.4736996
View Table of Contents: http://aip.scitation.org/toc/apl/101/2
Published by the American Institute of Physics

Design and measurements of an electrically small, broad bandwidth, non-Foster circuit-augmented protractor antenna

Ning Zhu and Richard W. Ziolkowski
Department of Electrical and Computer Engineering, University of Arizona, 1230 E. Speedway Blvd., Tucson, Arizona 85721-0104, USA

(Received 29 May 2012; accepted 28 June 2012; published online 13 July 2012)

A broad bandwidth, electrically small, metamaterial-inspired protractor antenna was designed, fabricated and tested around 300 MHz. Its broad bandwidth property was achieved by augmenting the protractor-shaped near-field resonant parasitic (NFRP) element with a non-Foster circuit. The resulting active NFRP element provided the means to surpass the fundamental passive limits. The measurement results for this non-Foster protractor antenna showed more than a 10 times increase of the 10 dB fractional bandwidth (FBW_{10dB}) of the original passive version. The corresponding half-power bandwidth (BW_{3dB}) was more than 8.24 times the passive upper bound. © *2012 American Institute of Physics*. [http://dx.doi.org/10.1063/1.4736996]

Electrically small antennas (ESAs) are one of the most researched topics in wireless systems today because they are a major enabling technology for advanced mobile platforms, which continue to emphasize more compact sizes and multi-functionality. An antenna is electrically small if its electrical size is much smaller than a wavelength at its operational/resonance frequency. More specifically, the commonly accepted definition of an ESA is $ka = 2\pi\,(a/\lambda) < 1$, where a is the radius of the smallest sphere enclosing the entire antenna system and λ is the free-space wavelength. For any electrical size and intended applications, there are always some trade-offs to consider among the important performance characteristics of an ESA, e.g., impedance matching to the source, radiation efficiency (*RE*), directivity, and bandwidth (BW) (or quality factor). A variety of metamaterial-inspired ESAs that exhibit high radiation efficiencies and nearly complete matching to a specified source have been designed, fabricated, and measured.[1–3] For example, the antennas in Ref. 1 are based on the electric and magnetic couplings between their driven elements and their near-field resonant parasitic (NFRP) elements. The NFRP elements act as near-field impedance transformers that match the antenna to the source without the need for any external matching network.

One of the major limitations of an ESA for any high data rate application is the fact that its bandwidth is small, a constraint arising from the basic radiation physics. The Chu-Thal limits[4,5] specify, for any ESA constructed with only passive elements, the lower bound on its quality factor and, hence, the upper bound on its bandwidth. In particular, the minimum quality factors for an isolated resonance of a magnetic and an electric antenna are $Q_{mag} = 2Q_{elec} = 3Q_{lb}$, where the realized lower bound $Q_{lb} = RE \times Q_{Chu}$ and $Q_{Chu} = 1/ka + 1/(ka)^3$ being the Chu lower bound. While it was heuristically known that having the antenna fill the enclosing spherical volume as much as possible led to the smallest Q values, recent theoretical efforts[6,7] have quantified this effect. For instance, the minimum quality factor for antennas which have basically a two-dimensional nature becomes $Q_{mag,planar} = 2Q_{elec,planar} = (3\pi/2)\ Q_{elec} \approx 7.07\ Q_{Chu}$.[7] Thus, based on the relationship between the half power VSWR fractional bandwidth (i.e., $FBW_{3dB} = BW_{3dB}/f_r$, f_r being the resonance frequency and BW_{3dB} being the 3dB bandwidth defined as: $BW_{3dB} = f_+ - f_-$, where $|S_{11}(f_+)| = |S_{11}(f_-)| = -3$ dB and $f_- < f_r < f_+$) and the quality factor, i.e., $FBW_{3dB} \approx 2/Q$, the maximum 3 dB bandwidth for a planar magnetic antenna in free space is

$$BW_{mag,planar} \approx \frac{8}{9\pi}\frac{1}{RE}\left[\frac{(ka)^3}{1+(ka)^2}\right] f_r. \tag{1}$$

Therefore, the largest bandwidth of a passive antenna is constrained by its *RE* and electrical size. This expression clearly shows the reason for a common practice—trading radiation efficiency for bandwidth, i.e., an antenna's bandwidth can be increased simply at the cost of increasing its losses and, hence, decreasing its *RE*. While a number of researchers have recently reported approaching the passive lower bounds with a variety of antenna structures (see, e.g., Refs. 1–3 and 7–10), the available fractional bandwidth even if the Chu lower bound is reached, is severely restricted when the electrical size is small. We note that the 10 dB bandwidth, BW_{10dB}, is defined in a similar manner but with the corresponding: −10 dB points.

On the other hand, it has been demonstrated (e.g., Refs. 11–14) that one can overcome these passive limits and achieve broadband ESAs, by introducing an active non-Foster element. Being different from traditional external non-Foster matching networks between the antenna and the source,[11,12] our approach incorporates the non-Foster circuit totally into the NFRP elements of the antennas.[13,14] This paper reports the experimental verification of this internal active matching element approach suggested for the protractor NFRP antenna.[14] The 300 MHz operating frequency was selected for a proof-of-concept design and simply to keep the physical size of the antenna and the frequency requirements on the lumped element components used in the non-Foster circuit reasonable.

The 300 MHz passive, electrically small, protractor antenna, shown in Fig. 1(a), was designed using ANSYS/ANSOFT'S High Frequency Structure Simulator (HFSS). It is

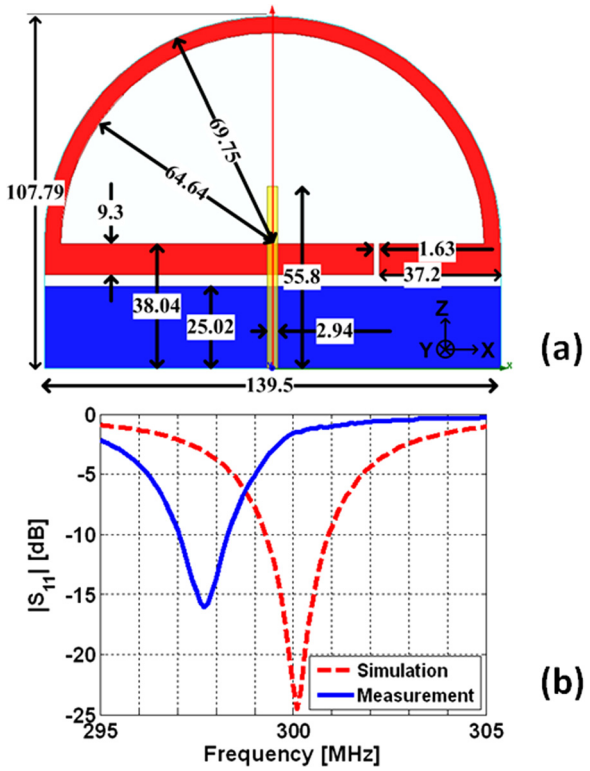

FIG. 1. Passive, 50 Ω, 300 MHz protractor antenna. (a) Side view. All dimensions are in mm. (b) Simulated and measured $|S_{11}|$ values.

based on the 0.5-oz (0.017 mm thick) copper, 31-mil Rogers Duroid™ 5880 substrate ($\varepsilon_r = 2.2$, $\mu_r = 1.0$, loss tangent = 0.0009) as the board material. The protractor-shaped capacitively loaded loop (CLL) NFRP element on the front side (red object) is driven by a monopole antenna on the back side (yellow object). The simulated $|S_{11}|$ values are shown in Fig. 1(b), yielding a −22.7 dB value at 300 MHz; a 1.6 MHz, 10 dB bandwidth (BW_{10dB}); and a 0.53% FBW_{10dB}. The simulated results also show a 1.46 dB peak gain and an 85.8% *RE* at 300 MHz. The protractor-shaped NFRP element is the main radiator at the resonance frequency. It is electrically coupled to the driven monopole antenna; the current induced on it is driven into a loop mode at resonance. Thus, the protractor antenna radiates as a small magnetic dipole antenna. With respect to the minimum quality factor, the Q-ratio for this planar magnetic NFRP antenna in free space is: $\text{Q-ratio} = Q_{3dB}/Q_{mag,\,planar} = Q_{3dB} \times BW_{mag,\,planar}/2f_r \approx 1.93$, when the simulated Q_{3dB} value of the passive protractor antenna is calculated with [Ref. 15, Eq. (96)].

Although the calculated Q-ratio is less than 2, meaning that the passive protractor antenna achieves a bandwidth which is about half of the maximum value defined by the refined Chu-Thal limit (1), the FBW_{10dB} is relatively small. In order to increase the bandwidth for wireless applications, an ideal frequency-dependent capacitor was incorporated first into the gap of the protractor-shaped NFRP element to investigate the frequency agility of the resulting antenna. As the capacitor value is tuned from 1.6 pF to −0.6 pF, the protractor antenna yields a broad bandwidth frequency response with the BW_{10dB} being more than 200 MHz. This behavior is illustrated in Fig. 2(a). The corresponding HFSS-predicted radiation efficiencies at the various resonance frequencies in Fig. 2(a) are shown in Fig. 2(b). The *RE* becomes a frequency-dependent characteristic because the much lower resonance frequencies decrease the *ka* value of the antenna sufficiently that the conductive and dielectric losses begin to dominate over the radiation losses. Because the requisite capacitance is decreasing with increasing frequency, a non-passive element, i.e., a non-Foster circuit, must be introduced in order to transform the frequency agile characteristics into an instantaneous bandwidth. Using the internal matching element approach, a negative impedance convertor (NIC) was designed for this purpose.[14] Prototype non-Foster negative capacitors with the desired negative slope characteristics have been experimentally validated for use in an ultra-broadband transmission line.[16] While there were two practical configurations of Linvill's NIC circuits[17] that could be implemented: the floating and grounded versions, the floating version was selected to match the frequency-dependent capacitance curve shown in Fig. 2(b) because neither of the two "horizontal" legs of the protractor NFRP element is connected to ground. These capacitance values were extracted from the corresponding resonance frequencies obtained in the frequency agile sweep results given in Fig. 2(a).

A low noise NPN silicon bipolar transistor (Avago AT41511) was selected as the basis for the NIC circuit. While both BJT and FET devices were considered, the high performance characteristics of BJTs were attractive. In order to achieve the steep slope of the capacitance curve shown in Fig. 2(b), a series L-C structure was selected to connect the bases of the two transistors. This combination replaces the single component design reported previously;[17] it provided

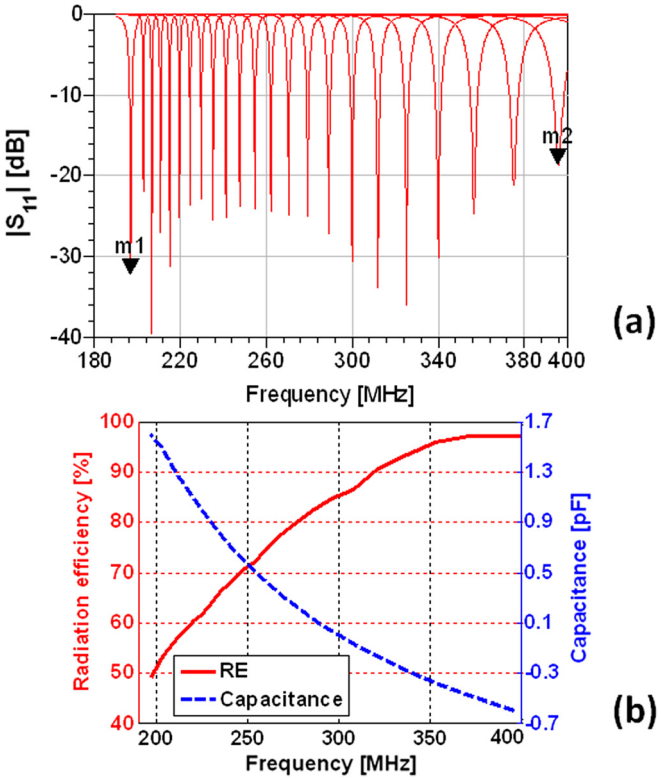

FIG. 2. Passive frequency agile protractor antenna system. (a) $|S_{11}|$ values versus frequency as the capacitance across the NFRP gap varies from 1.6 pF (m1, $f_r = 196.9$ MHz, $|S_{11}| = -32.2$ dB) to −0.6 pF (m2, $f_r = 395.8$ MHz, $|S_{11}| = -18.6$ dB), and (b) the corresponding simulated resonance frequency and radiation efficiency values.

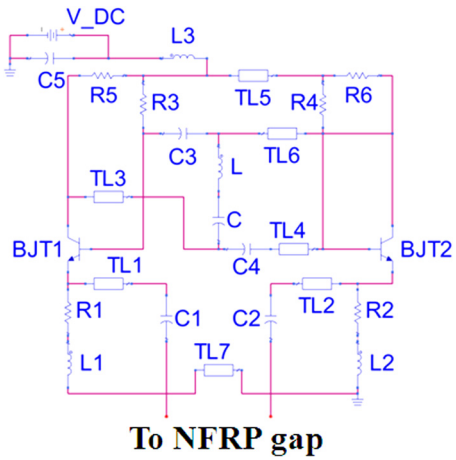

FIG. 3. Revised floating two-port NIC circuit for our protractor antenna. R1 = 85.6 Ω, R2 = 298 Ω, R3 = 4.3 kΩ, R4 = 68.1 kΩ, R5 = 82 Ω, R6 = 583 Ω, C = 82 pF, C1 = 6.8 pF, C2 = 82 pF, C3 = 82 pF, C4 = 82 pF, C5 = 10 nF, L = 220 nH, L1 = 11 nH, L2 = 82 nH, L3 = 330 nH, TL1 = 1 mm, TL2 = 2.5 mm, TL3 = 9.5 mm, TL4 = 6 mm, TL5 = 1 mm, TL6 = 8 mm, TL7 = 22 mm, and V_DC = 7.97 V. The width of all transmission lines is 1 mm.

more adjustability to the design. Moreover, instead of the original symmetric direct current (DC) bias structure introduced by Linvill[17] and used by us previously,[14] this asymmetric structure provided more tunability to achieve the requisite high reactance slope. The length and connection of the transmission lines that could affect the NIC circuit performance were determined first to obtain a more accurate electromagnetic (EM) model of the whole antenna system. The revised NIC circuit model for the protractor antenna is shown in Fig. 3. Although neither of the two legs of the NIC circuit connects directly to DC or to ground, the capacitors C1 and C2 are required to separate the DC signals between the emitters of the two transistors. The series L-C structure; the resistors: R1, R2; and the inductors: L1, L2, which play a significant role in achieving the non-Foster capacitance behavior, are the most sensitive component values in the NIC circuit.

To develop an understanding of the EM and parasitic capacitance and inductance effects of the transmission line on the protractor antenna performance, Agilent's advance design system (ADS) EM simulator, Momentum, was used to simulate the protractor antenna simultaneously with the NIC circuit's transmission lines. As shown in Fig. 4(a), 5 ports were defined in Momentum. Ports 1 and 2 were connected to the 50 Ω radio frequency (RF) source. Ports 3 and 4 were connected to the two legs of the floating NIC circuit: port 3 to the capacitor C1 and port 4 to the capacitor C2 indicated in Fig. 3. The intermediate port 5 was added as a reference for ports 3 and 4; it physically decreased the distance between them. The Momentum simulations showed physically reasonable passive behaviors in agreement with the HFSS results.

With the Momentum-simulated EM model of the protractor antenna augmented with the NIC circuit, the floating two-port NIC circuit was co-designed and optimized systematically in the ADS simulations to maximally expand the antenna's BW_{10dB}, centered near 300 MHz. In these simulations, the two transistors were optimized to work at their forward active region, which means their base voltages were assumed larger than their emitter voltages, but smaller than

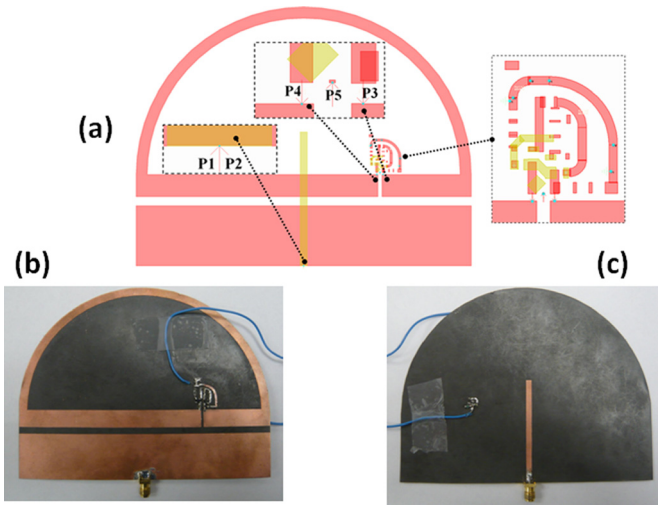

FIG. 4. NIC-augmented protractor antenna. (a) 5-port ADS Momentum simulation model, and (b) front view and (c) back view of the fabricated system.

their collector voltages. The two collector currents were restricted to being less than the maximum value reported in their datasheet. The simulation results of the expanded BW_{10dB} are shown in Fig. 5. An 87.9 MHz bandwidth, from 257.2 to 345.1 MHz was obtained. Note that we used the S-parameter files for all of the inductors and capacitors, which were obtained experimentally with a standard transmission line configuration, to achieve these more accurate simulation results. As shown in Fig. 5, even larger bandwidths were predicted originally using only the ideal lumped elements values. However, it was found experimentally that the component information provided by the vendors was totally inadequate to predict the actual behavior of such a highly optimized nonlinear circuit. The fluctuations in the simulated BW_{10dB} observed in Fig. 5 are a consequence of using the measured frequency-dependent S-parameters of the capacitors and inductors. They are not instability oscillations. Note that the commercially provided capacitor, inductor, and resistor values are reported in Fig. 3.

The fabricated protractor antenna is presented in Figs. 4(b) and 4(c). Without any lumped element components, the $|S_{11}|$ values of the original protractor antenna with the presence of the NIC circuit's transmission lines were measured with an Agilent E8361A vector network analyzer (VNA). We used RF ferrite chokes provided by Wurth Electronics to

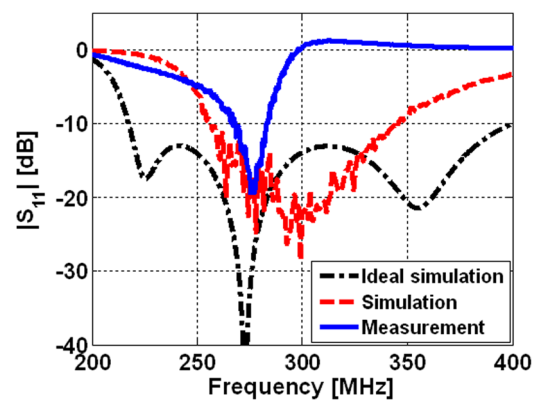

FIG. 5. Simulated and measured $|S_{11}|$ values versus frequency for the non-Foster circuit augmented protractor antenna.

eliminate any cable effects on the augmented protractor antenna. These measured values are compared to the HFSS simulation values of the antenna alone in Fig. 1(b). One observes that the resonance frequency is down-shifted by only 2.3 MHz when the NIC circuit's transmission lines are present. These measurements also confirmed the matching of the basic antenna structure to the 50 Ω source.

Considerable efforts were put into the measurements to achieve the broadband non-Foster protractor antenna results experimentally. The largest BW_{10dB} we obtained in the measurements was 14.8 MHz, as shown in Fig. 5. This represents a 5.4% FBW_{10dB} for the resulting resonance frequency, 275.5 MHz, for this $ka = 0.444$ antenna. Compared to the original passive protractor antenna, this represents a measured 10.1 times increase in its FBW_{10dB}. Although we did not have the means to measure *RE*, we know approximately its value from the various simulations. The corresponding measured BW_{3dB} at 275.5 MHz is still more than 8.24 times the upper bound (1) when the simulated value: $RE = 79.5\%$, obtained from Fig. 2(b) for $f_r = 275.5$ MHz, is taken into account.

There are several reasons which caused non-trivial difficulties in obtaining accurate $|S_{11}|$ values for comparisons between the simulations and measurements. The performance of the non-Foster protractor antenna is very sensitive to the active NIC circuit. Although more accurate measured S-parameter models of the passive components were incorporated in the final NIC circuit simulations, the 5% tolerance of the lumped element values made the measurements difficult. As a result, we had to do a manual optimization with the available component values during the measurements. Tunable lumped elements would have decreased significantly the difficulties in this fine tuning process. In order to achieve the realized large BW_{10dB} centered near 300 MHz, extreme care had to be exercised when the capacitance value crossed 0 pF. The associated large variations in the reactance caused non-trivial experimental difficulties with the operation of the NIC circuit. Moreover, the transistor model was another significant issue. The vendors provided S-parameter models of their transistors; it was found to be more accurate in their advertised low noise amplifier application. Similar models were not available for this particular NIC circuit application. The ADS equivalent circuit model for the transistor was the only available model for our RF case. We have found that the discrepancies between the S-parameters simulated by the ADS equivalent circuit model and the S-parameter values provided by the vendors caused many of the differences between the simulation and measurement results for our design. Furthermore, the impact of the DC power and ground wires connected to the NIC circuit could not be included well in the simulations. They had a small but noticeable impact on the measured resonance frequency and bandwidth. Finally, stability is always an important and interesting issue in any non-Foster circuit design. In the simulation, we have checked the stability for the whole antenna system, including the NIC circuit, in the frequency band of interest using the ADS Transient simulator. The simulations showed that the system is stable from 200 to 400 MHz. However, stability issues did cause difficulties in the measurements. We were able to overcome many of these by decreasing the DC bias voltages experimentally and, hence, the base current values.

We have reported a proof-of-concept design of an electrically small antenna augmented with an internal non-Foster circuit to increase its bandwidth. Moreover, we reported the experimental verification that this approach achieved more than a 10-fold increase of its FBW_{10dB}. Although there are non-trivial practical difficulties to achieve the theoretically possible very large bandwidths shown in our ideal simulations, specialized components or integrated circuit versions of the NIC circuit,[18] as well as more accurate models of the transistor and lumped elements with acceptable tolerances, could lead to improved practical implementations in the future.

For the active radiating system design and its experimental validation, we produced *RE* values based on RF simulations that included only the passive structures. To calculate its actual overall efficiency, the DC power consumption in both the passive and active components must be taken into account. The DC power consumption plays a crucial role in any practical mobile device, particularly since its energy storage component must provide for not only the radiated power but also the power driving an increasing number of amplifier-based sub-systems. Moreover, amplified circuit power can lead to amplified radiated power and, hence, to *RE* values greater than 1 with standard definitions. We are currently investigating various aspects of how one could define the overall efficiency in the presence of both passive and active components in a radiating system and hope to report on these issues in the near future.

This work was supported in part by NSF Contract No. ECCS-1126572. The authors would like to thank Dr. David Cox, ECE Department, University of Arizona, for his time and efforts in checking our circuit models and their stability and suggesting improvements in their experimental realizations. The authors would like to thank American Technical Ceramics Corp., Avago Tech., Coilcraft, Vishay, and Wurth Electronics for their generous donations of samples that made these experiments possible.

[1]R. W. Ziolkowski, P. Jin, and C.-C. Lin, Proc. IEEE **99**, 1720 (2011).
[2]H. Mirzaei and G. V. Eleftheriades, IEEE Antennas Wireless Propag. Lett. **10**, 1154 (2011).
[3]Y. Dong and T. Itoh, Proc. IEEE **100**, 2271 (2012).
[4]L. J. Chu, J. Appl. Phys. **19**, 1163 (1948).
[5]H. L. Thal, IEEE Trans. Antennas Propag. **54**, 2757 (2006).
[6]M. Gustafsson, C. Sohl, and G. Kristensson, IEEE Trans. Antennas Propag. **57**, 1319 (2009).
[7]A. D. Yaghjian and H. R. Stuart, IEEE Trans. Antennas Propag. **58**, 3114 (2010).
[8]S. R. Best, IEEE Trans. Antennas Propag. **53**, 1047 (2005).
[9]O. S. Kim, O. Breinbjerg, and A. D. Yaghjian, IEEE Trans. Antennas Propag. **58**, 1898 (2010).
[10]D. F. Sievenpiper, D. C. Dawson, M. M. Jacob, T. Kanar, S. Kim, J. Long, and R. G. Quarforth, IEEE Trans. Antennas Propag. **60**, 8 (2012).
[11]S. E. Sussman-Fort and R. M. Rudish, IEEE Trans. Antennas Propag. **57**, 2230 (2009).
[12]J. T. Aberle, IEEE Trans. Antennas Propag. **56**, 1218 (2008).
[13]P. Jin and R. W. Ziolkowski, IEEE Trans. Antennas Propag. **58**, 318 (2010).
[14]N. Zhu and R. W. Ziolkowski, IEEE Antennas Wireless Propag. Lett. **10**, 1582 (2011).
[15]A. D. Yaghjian and S. R. Best, IEEE Trans. Antennas Propag. **53**, 1298 (2005).
[16]S. Hrabar, I. Krois, I. Bonic, and A. Kiricenko, Appl. Phys. Lett. **99**, 254103 (2011).
[17]J. G. Linvill, Proc. IRE **41**, 725 (1953).
[18]C. R. White, J. W. May, and J. S. Colburn, IEEE Microw. Wirel. Compon. Lett. **22**, 35 (2012).